Mon. Not. R. Astron. Soc. **341,** 792–804 (2003)

Detecting X-ray filaments in the low-redshift Universe with *XEUS* and *Constellation-X*

M. Viel,[1,2⋆] E. Branchini,[3⋆] R. Cen,[4⋆] S. Matarrese,[1,5⋆] P. Mazzotta[6⋆] and J. P. Ostriker[2⋆]

[1]*Dipartimento di Fisica 'Galileo Galilei', via Marzolo 8, I-35131 Padova, Italy*
[2]*Institute of Astronomy, Madingley Road, Cambridge CB3 0HA*
[3]*Dipartimento di Fisica, Università di Roma TRE, Via della Vasca Navale 84, 00146 Roma, Italy*
[4]*Princeton University Observatory, Princeton University, Princeton, NJ 08544, USA*
[5]*INFN, Sezione di Padova, via Marzolo 8, I-35131 Padova, Italy*
[6]*Department of Physics, University of Durham, South Road, Durham DH1 3LE*

Accepted 2003 January 20. Received 2002 December 17; in original form 2002 October 22

ABSTRACT

We propose a possible way to detect baryons at low redshifts from the analysis of X-ray absorption spectra of bright AGN pairs. A simple semi-analytical model to simulate the spectra is presented. We model the diffuse warm–hot intergalactic medium (WHIM) component, responsible for the X-ray absorption, using inputs from high-resolution hydrodynamical simulations and analytical prescriptions. We show that the number of O VII absorbers per unit redshift with column density larger than $10^{13.5}$ cm^{-2} – corresponding to an equivalent width of $\sim$1 km s^{-1} – that will possibly be detectable by *XEUS*, is $\gtrsim$30 per unit redshift. *Constellation-X* will detect $\sim$6 O VII absorptions per unit redshift with an equivalent width of 10 km s^{-1}. Our results show that, in a ΛCDM universe, the characteristic size of these absorbers at $z \sim 0.1$ is $\sim 1\ h^{-1}$ Mpc. The filamentary structure of WHIM can be probed by finding coincident absorption lines in the spectra of background AGN pairs. We estimate that at least 20 AGN pairs at separation $\lesssim$20 arcmin are needed to detect this filamentary structure at the 3σ level. Assuming observations of distant sources using *XEUS* for exposure times of 500 ks, we find that the minimum source flux to probe the filamentary structure is $\sim 2 \times 10^{-12}$ erg cm^{-2} s^{-1} in the 0.1–2.4 keV energy band. Thus, most pairs of these extragalactic X-ray bright sources have already been identified in the *ROSAT* All-Sky Survey. Re-observation of these objects by future missions could be a powerful way to search for baryons in the low-redshift Universe.

Key words: intergalactic medium – quasars: absorption lines – cosmology: theory – large-scale structure of Universe.

1 INTRODUCTION

The census of baryons in the low-redshift Universe shows that a large fraction of them has not been detected yet. While almost 80 per cent of the baryons reside in the Lyα forest at $z \sim 2$ (Rauch 1998), estimates at lower redshift imply that the observed baryon density is significantly lower (Fukugita, Hogan & Peebles 1998; Nicastro et al. 2002b) and does not match the nucleosynthesis constraints (Burles & Tytler 1998). Hydro-dynamical simulations suggest that a large fraction of baryons at $z \sim 0$ could be in a warm–hot intergalactic medium (WHIM), with a temperature between 10^5 and 10^7 K and with moderate overdensities $\Delta \sim$ 10–100 (Ostriker & Cen 1996; Cen & Ostriker 1999a; Cen et al. 2001; Davé et al. 2001). Detection of this component is particularly difficult and requires very sensitive UV and X-ray satellites.

Recently, various attempts to model analytically the WHIM component have been made. Perna & Loeb (1998) used the Press & Schechter theory (Press & Schechter 1974) and an isothermal model for the gas component to address the detectability in absorption of the hot and highly ionized intergalactic medium (IGM) that resides in the outskirts of clusters and groups of galaxies. Valageas, Schaeffer & Silk (2002) showed that the temperature–density relation found in hydrodynamical simulations can be reproduced using straightforward physical arguments. In this simple picture, the IGM consists of two phases: the cool photo-ionized component, which gives rise to the Lyα forest, and the WHIM, which is dominated by shock heating.

⋆E-mail: viel@pd.infn.it (MV); branchini@fis.uniroma3.it (EB); cen@astro.princeton.edu (RC); matarrese@pd.infn.it (SM); mazzotta@durham.ac.uk (PM); jpo@ast.cam.ac.uk (JPO)

Hydro-dynamical simulations of structure formation in the context of cold dark matter models have been the major contribution to the theoretical understanding of the WHIM. Hellsten, Gnedin & Miralda-Escudé (1998), referred to the network of filaments and sheet-like structures, possibly seen in the spectra of background bright sources in the X-ray band, as the 'X-ray forest', in analogy with the Lyα forest. Their main result is that O VII and O VIII absorptions by the intervening IGM can be seen by future X-ray missions. Cen et al. (2001) used large box-size hydrodynamical simulations to detect O VI absorption by the WHIM in the UV band and find results in reasonably good agreement with observations. Fang, Bryan & Canizares (2002a) performed hydrodynamical simulations to study the metal distribution in the IGM and, assuming collisionally ionized gas, compared their results with semi-analytical models based on the Press & Schechter formalism. Kravtsov, Klypin & Hoffman (2002) addressed WHIM detectability using hydrodynamical simulations to model the gas distribution in the Local Supercluster region and imposing constraints from the MARK III catalogue of galaxy peculiar velocity.

More recently, Chen et al. (2002) have made an extensive study of the detectability of O VII and O VIII absorbers using the $z = 0$ output of a hydrodynamical simulation of a ΛCDM universe, and assuming a uniform metallicity of 0.1 solar for the IGM. Their results confirm that the detectability of these absorbers is challenging. It has been shown that the number of intervening O VI absorbers per unit redshift is quite high at low redshift (Tripp, Savage & Jenkins 2000). Thus, a very promising technique to detect O VII and O VIII systems is to search at the redshift of known O VI systems in the spectra: this allows one to lower the S/N ratio needed for O VII and/or O VIII detectability. Nicastro et al. (2002a) presented the X-ray 5σ-level detection by *Chandra* of a resonant absorption from WHIM along the line of sight towards the blazar PKS 2155-304. Moreover, Fang et al. (2002b) reported the detection of an O VIII absorption line along the sight-line towards PKS 2155-304 with *Chandra*. They constrained the gas that gives rise to this line to have an overdensity in the range 30–350 and a temperature of 4–5 $\times$ 10^6 K, in agreement with hydro-simulations. Emission by the WHIM could also be important and several models have been proposed (e.g. Scharf et al. 2000; Phillips, Ostriker & Cen 2001; Zappacosta et al. 2002). Here, we will focus on absorption: the bulk of the missing baryons should reside in a medium which is too rarefied to be detectable through its X-ray emission or Sunyaev-Zel'dovich effect (Ostriker & Cen 1996).

These very recent observations are very encouraging and show that we have just started to detect the first 'trees' of the X-ray forest. Future X-ray missions such as *XEUS* and *Constellation-X* will be much more accurate a probe of the current cosmological models and will allow a detailed study of WHIM properties.

In this paper we will present a semi-analytical technique to simulate X-ray absorption spectra. There are two advantages in using a semi-analytical technique instead of the more accurate hydrodynamical simulations. First, semi-analytical models are not computationally expensive and are not limited by resolution and box-size effects. Secondly, semi-analytical techniques can be very efficient when coupled with detailed hydrodynamical simulations when the latter can be used to calibrate the former and allow one to explore the parameter space very quickly. For example, it will be straightforward to study the effects of the metallicity of the IGM, different UV and X-ray backgrounds, scatter in the temperature–density and in the metallicity–density relation, peculiar velocities, etc. For the estimates we want to make here, semi-analytical techniques, which use the inputs of hydrodynamical simulations, will be shown to be successful in reproducing potentially observable quantities such as the column densities of O VII and O VIII absorbers.

In particular, we will focus on the simulations of absorption spectra of AGN pairs and we will try to determine the characteristic size of the absorbers by identifying absorption features in the simulated spectra. The estimate of the extent of the absorbers, using the information contained in the transverse direction, could be a very powerful probe of the filamentary network of the WHIM. An extensive analysis of the correlations of Lyα clouds at $z > 2$ using hydrodynamical simulations has been made in Miralda-Escudé et al. (1996) and Cen & Simcoe (1997). McGill (1990), Crotts et al. (1994), Bechtold et al. (1994) and Charlton et al. (1997) performed similar analysis for observed Lyα clouds and showed that the coherence length in the transverse direction of the clouds could be significantly larger than the size of a single cloud. This argument has been clarified recently using simple physical arguments (Schaye 2001) and hydrodynamical simulations (e.g. Theuns et al. 1998), which indeed show that the clouds are embedded in a network of filaments. The idea is very simple: while a single line of sight (LOS) allows one to probe only the size of a single absorber, pairs of LOSs are sensitive to the random orientation of the filaments and diffuse blobs and can better sample the WHIM. Another advantage of using the information contained in a sample of pairs is that this method minimizes the contamination of the WHIM signal we have to detect with the intrinsic lines of the background source. This is due to the fact that the positions of the intrinsic absorption or emission features of the source along the LOS are random. Thus, their effect can be statistically modelled and removed as has been done recently to recover the linear dark matter power spectrum from simulated Lyα absorptions (Viel et al. 2002a).

The outline of the paper is as follows. In Section 2 we describe the ingredients needed to simulate the X-ray AGN spectra focusing both on the inputs from hydrodynamical simulations (Subsection 2.1) and on analytical modelling (Subsection 2.2). In Section 3 we test how well the semi-analytical model matches the properties of simulated lines extracted directly from hydro-simulations. This comparison is done in terms of the predicted number counts of absorbers per unit redshift range. In Section 4 we discuss a possible way to recover the characteristic size of these absorbers by using the so-called 'hits-and-misses' statistics and discuss the detectability of these absorption features by satellites of the next generation such as *XEUS* and *Constellation-X*. Section 5 contains our main conclusions.

2 SEMI-ANALYTICAL MODEL OF THE X-RAY FOREST

This Section presents the semi-analytical method used to simulate the X-ray spectra of AGNs. In Subsection 2.1 we present the hydrodynamical simulation used, focusing on the basic ingredients that will constitute the inputs for the semi-analytical model: (i) the probability distribution function (pdf) of the gas; (ii) the gas metallicity–density relation; (iii) the gas temperature–density relation; (iv) the X-ray background. In Subsection 2.2 we describe in detail the technique used, with the relative mathematical implementation (see also Appendix A), to produce the simulated spectra of AGN pairs.

2.1 Model parameters from hydrodynamical simulations

The hydrodynamical simulation used here is a ΛCDM model with the following parameters: $H_0 = 100\,h$ km s^{-1} Mpc^{-1} with $h =$

0.67, $\Omega_{0m} = 0.30$, $\Omega_{0b} = 0.035$, $\Lambda = 0.70$, $\sigma_8 = 0.90$, and the spectral index of the primordial power spectrum $n = 1$. The box-size of the simulation is 25 comoving h^{-1} Mpc on a uniform mesh with 768^3 cells. The comoving cell size is 32.6 h^{-1} kpc and the mass of each dark matter particle is $\sim 2 \times 10^7$ $M_\odot$ (further details can be found in Cen et al. 2001). The simulation includes galaxy and star formation, energy feedback from supernova explosions, ionization radiation from massive stars and metal recycling due to SNe/galactic winds. Metals are ejected into the local gas cells where stellar particles are located using a yield $Y = 0.02$ and are followed as a separate variable adopting the standard solar composition (some slices through the simulation box at various redshift outputs can be found at http://astro.Princeton.EDU/∼cen/PROJECTS/p2/p2.html).

To simulate X-ray absorptions properly, we have to know the actual X-ray and UV background of the simulation at $z = 0$, which is computed self-consistently given the sinks and the sources in the simulation box. We have checked that there are very small differences between the hydro-simulation background and the estimate from Shull et al. (1999): $I_{\rm UV} = I^0_{\rm UV}\ (E/13.6\ {\rm eV})^{-1.8}$, with $I^0_{\rm UV} = 2.3 \times 10^{-23}$ erg cm^{-2} Hz^{-1} sr^{-1} s^{-1} for the UV background (which includes a contribution from AGNs and starburst galaxies), and $I_X = I^0_X (E/E_X)^{-1.29}\ \exp\ (-\ E/E_X)$, with $I^0_X = 1.75 \times 10^{-26}$ erg cm^{-2} Hz^{-1} sr^{-1} s^{-1} and $E_X = 40$ keV (Boldt 1987; Fabian & Barcons 1992; Hellsten et al. 1998; Chen et al. 2002), for the X-ray background. The difference between the amplitude of the UV and X-ray background of the hydro-simulations and the estimates above is less than a factor of 2, in the range $0.003 \lesssim$ E (keV) $\lesssim 4$. In Fig. 1 we plot the X-ray and UV background of the hydro-simulations at $z = 0$ (dashed line), the estimates of Shull et al. (1999) (long-dashed line) and Fabian & Barcons (1992) (dot–dashed line), and the sum of these two (continuous line).

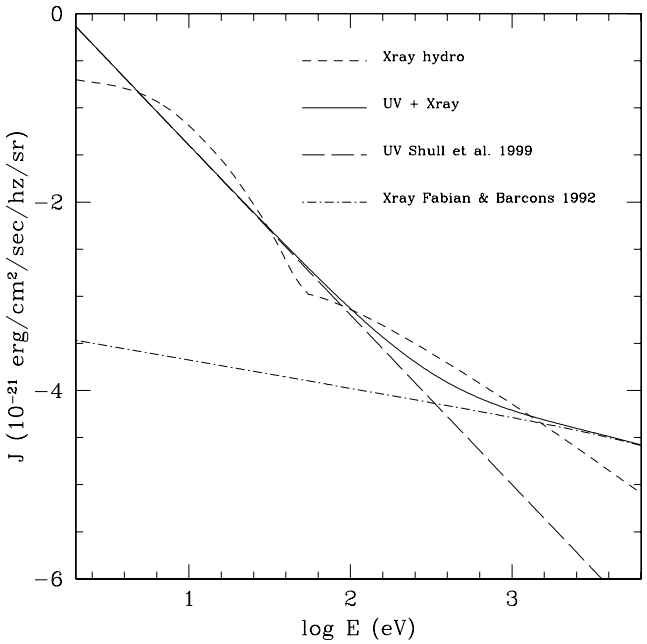

Figure 1. The X-ray and UV background. The short-dashed line shows the background extracted from the $z = 0$ output of the hydrodynamical simulations and used to compute our spectra. The estimates of Shull et al. (1999) for the UV background are represented by the long-dashed line. The results of Fabian & Barcons (1992) for the X-ray background are also reported (dot–dashed line). The sum of the latter two is represented by the continuous line.

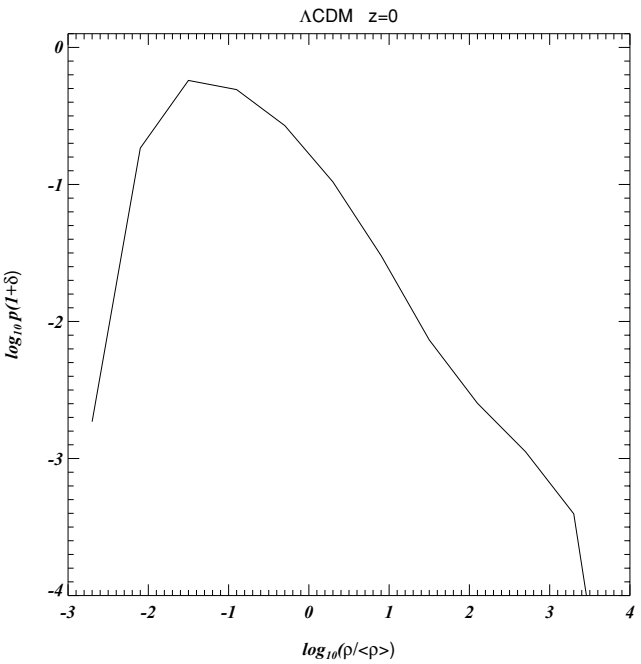

Figure 2. Probability distribution function of the gas overdensity for the $z = 0$ output of the ΛCDM model.

Of the two backgrounds, the X-ray background plays a major role in determining the statistics of the simulated spectra. We will assume that the amplitude of the ionizing backgrounds scales like $(1 + z)^3$, in the redshift range $0 < z < 1$. This assumption will not influence significantly our results: given the fact that we will generate mock-spectra at $z < 0.3$, this will determine a scaling of the amplitude by a factor of less than 2.

Along many randomly chosen sight-lines parallel to one of the axes of the simulation box, we compute the gas density and peculiar velocity, the gas temperature, and the metal density. This allows us to obtain a sample of 1000 simulated absorption spectra.

From the $z = 0$ output we extract the pdf of the gas density, which is shown in Fig. 2, this will be implemented in the semi-analytical (hereafter SA) model. Starting from the linear density field, generated with the right correlation properties predicted by linear theory (Subsection 2.2), we assign each pixel a new non-linear density in such a way that the resulting non-linear pdf is that extracted from hydrodynamical simulations.

The gas density–temperature relation is shown in panel (a) of Fig. 3, where we report the mean value in each density bin and the scatter. This result is in reasonable agreement with the recent results obtained by Yoshida et al. (2002, their fig. 2) and also by Davé et al. (1999), who studied the gas cooling processes in the framework of smoothed particle hydro-dynamics (SPH) simulations. We note that the scatter in temperature can be very high for values of $\log\ (1 + \delta) > -1$, spanning more than one order of magnitude. We report the gas density–metallicity relation in panel (b). The trend here is as expected: low-density regions are the most metal poor, while at large densities the metallicity can be solar. In this plot the scatter is extremely large for the intermediate density regime, i.e. $-1 < \log\ (1 + \delta) < 0.5$, while it is significantly smaller for larger overdensities. This plot has to be compared with similar plots shown in Cen & Ostriker (1999b), but we find that here the scatter is somewhat larger than in previous simulations.

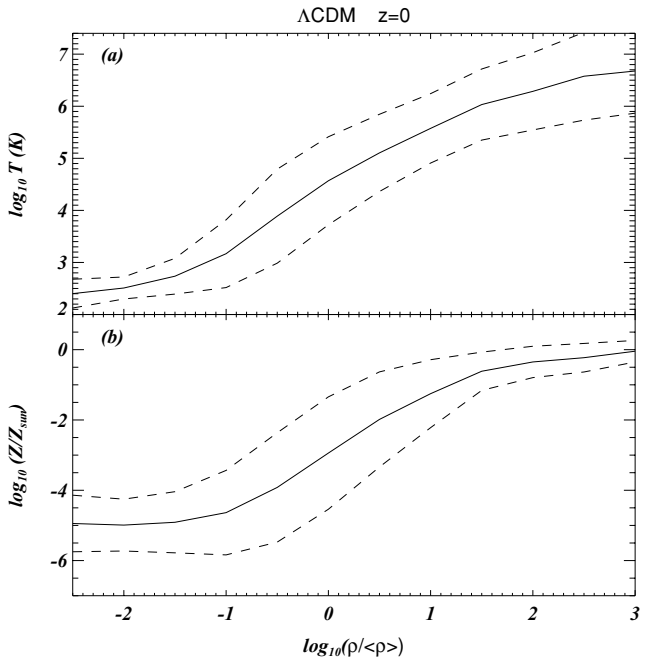

Figure 3. Panel (a) shows the temperature–density relation for the gas component, while panel (b) shows the metallicity as a function of density. The continuous lines represent the mean value in each bin, the dashed lines represent the scatter (1σ values). The quantities shown are volume weighted.

These curves, with their relative scatter assumed to be drawn from a Gaussian distribution, will be implemented into the SA model.

2.2 Simulation of absorption features in X-ray spectra of AGN pairs

We start here from the model introduced by Bi and collaborators (Bi, Börner & Chu 1992; Bi 1993; Bi, Ge & Fang 1995; Bi & Davidsen 1997 – hereafter BD97) for generating a Lyα absorption spectrum along a line of sight. This simple model predicts many properties of the absorption lines, including the column-density distribution and the distribution of linewidths (b parameters), which can be directly compared with observations.

The BD97 model is based on the assumption that the low-column-density Lyα forest is produced by smooth fluctuations in the intergalactic medium that arise as a result of the gravitational growth of perturbations. Linear density perturbations in the intergalactic medium $\delta^{\rm IGM}{}_0$ ($\boldsymbol{x}$, z) are related to the underlying linear dark matter (DM) perturbations by a convolution, which models the effects of gas pressure. In Fourier space one has: $\delta_0^{\rm IGM}(\boldsymbol{k}\ ,\ z) = W_{\rm IGM}(k,\ z)\ D_+(z)\ \delta_0^{\rm DM}(\boldsymbol{k})$, where $D_+(z)$ is the growing mode of density perturbations (normalized so that $D_+(0) = 1$) and $\delta_0^{\rm DM}(\boldsymbol{k})$ is the Fourier transformed DM linear over-density at $z = 0$. A commonly-adopted low-pass filter is $W_{\rm IGM}(k,\ z) = (1 + k^2/k^2{}_J)^{-1}$, which depends on the comoving Jeans wavelength $\lambda_J(z) \equiv 2\pi\ H_0^{-1}\{[2\ \gamma\ k_{\rm B}\ T_m(z)]/[3\ \mu\ m_p\ \Omega_{0\rm m}\ (1 + z)]\}^{1/2}$, where $k_{\rm B}$ is Boltzmann's constant, T_m the gas temperature, μ the molecular weight and γ the ratio of specific heats. $\Omega_{0\rm m}$ is the present-day matter density parameter. BD97 adopt a simple lognormal transformation to obtain the IGM density in the mildly non-linear regime from the linear one.

Several approximations are involved in this modelling. A first point which can be important is that the Jeans wavelength depends on density and temperature, and therefore Jeans smoothing should be an adaptive smoothing of the density field, while the Fourier implementation cannot take into account this local aspect (Viel et al. 2002b). In addition, a filtering of the dark matter density field at the Jeans scale may be not very accurate: different filtering functions result in very different gas-density fields and the real 'filtering scale' that better reproduces the gas distribution in the linear regime depends on the thermal history of the IGM (Gnedin & Hui 1998; Gnedin et al. 2003; Matarrese & Mohayaee 2002).

The modelling of the gas component using the lognormal transformation and a smoothing at the Jeans wavelength would determine a poor description of the gas distribution at $z \sim 0$, where the density fluctuations are in the non-linear regime. Even the tight relation between density and temperature for the gas responsible of Lyα absorption is no longer valid for the warm–hot intergalactic medium. In this case, hydro-simulations suggest that the scatter in the T–δrelation for the WHIM can be very large (Davé et al. 1999; Yoshida et al. 2002).

At least three inputs, taken from hydrodynamical simulations, can be used to improve the model: (i) the probability distribution function (pdf) of the gas density; (ii) the gas density–temperature relation; (iii) the gas density–metallicity relation. Viel et al. (2002b) showed that, by directly using the pdf of the gas density extracted from the hydrodynamical simulations, the pdf of the flux predicted by the semi-analytical model is in significantly better agreement with that predicted by hydro-simulations. The other two inputs allow one to take into account the physical state (temperature and metallicity) of the structures responsible for the absorptions.

Here we will follow closely the prescriptions used in Viel et al. (2002a,b). The modelling is based on the generation in Fourier space of 1D density and velocity fields, with the right correlation properties predicted by the theory.

Starting from a linear power spectrum $P(k)$ we generate 1D LOS linear random fields for the IGM density and peculiar velocity, with the low-pass filter window function $W_{\rm IGM}$. If we draw an LOS in the $x_\parallel$ direction at a fixed coordinate $x_\perp$, the Fourier component at redshift z of the linear density contrast and of the linear peculiar velocity field of the intergalactic medium (IGM) along the LOS are:

$$\delta_{0\parallel}^{\rm IGM}(k_\parallel, z|\boldsymbol{x}_\perp) = D_+(z) \int \frac{{\rm d}^2k_\perp}{(2\pi)^2} e^{i\boldsymbol{k}_\perp\cdot\boldsymbol{x}_\perp} \times W_{\rm IGM}\left(\sqrt{k_\parallel^2 + k_\perp^2}, z\right) \delta_0^{\rm DM}(k_\parallel, \boldsymbol{k}_\perp), \quad (1)$$

$$v_\parallel^{\rm IGM}(k_\parallel, z|\boldsymbol{x}_\perp) = ik_\parallel E_+(z) \int \frac{{\rm d}^2k_\perp}{(2\pi)^2} e^{i\boldsymbol{k}_\perp\cdot\boldsymbol{x}_\perp} \frac{1}{k_\parallel^2 + k_\perp^2} \times W_{\rm IGM}(\sqrt{k_\parallel^2 + k_\perp^2}, z)\delta_0^{\rm DM}(k_\parallel, \boldsymbol{k}_\perp), \quad (2)$$

with $E_+(z) = H(z)f(\Omega_{\rm m}\ ,\ \Omega_\Lambda)D_+(z)/(1 + z)$. Here $f(\Omega_{\rm m},\ \Omega_\Lambda) \equiv -{\rm d}\ \ln\ D_+(z)/\ {\rm d}\ \ln(1 + z)$, and $\Omega_{\rm m}$ and Ω_Λ are the matter and vacuum-energy contributions to the cosmic density (e.g. Lahav et al. 1991), respectively; $H(z)$ is the Hubble parameter at redshift z: $H(z) = H_0[\Omega_{0\rm m}(1 + z)^3 + \Omega_{0r}(1 + z)^2 + \Omega_{0\Lambda}]^{1/2}$, with $\Omega_{0r} = 1 - \Omega_{0\rm m} - \Omega_{0\Lambda}$. In our case we use the ΛCDM parameters of the previous subsection.

We then simulate the corresponding density and peculiar velocity at a distance $r_\perp$ from the first LOS. The correlation properties between these four fields are computed using an algebraic implementation, as described in Appendix A.

The linear density field is mapped into the non-linear one by directly using the pdf of the gas distribution obtained from hydro-simulations. This has been done with a rank-ordering technique between the linear density field and the non-linear one, which

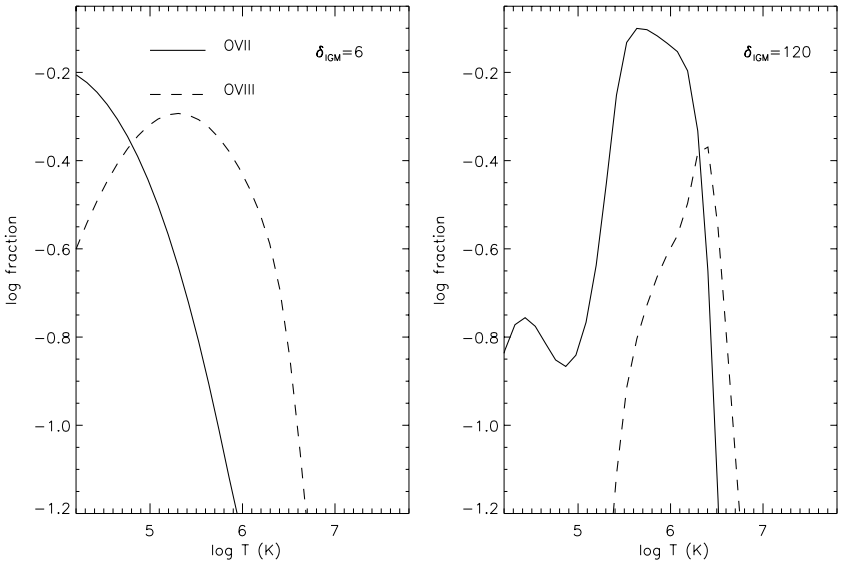

Figure 4. Logarithm of the ionization fraction as a function of gas temperature for O VII (continuous line) and O VIII (dashed line). The left-hand panel shows the results obtained with CLOUDY for an IGM overdensity $\delta = 6$, while in the right-hand panel the results are for an overdensity $\delta = 120$.

intrinsically consists in a monotonic and deterministic mapping of each generated field. To account for the scatter, we assign to each pixel a new temperature and metallicity value by adding to the mean value (continuous lines of Fig. 3) a random number taken from a Gaussian distribution with the same standard deviation as the hydro-simulations.

Peculiar velocities are approximated by those predicted by linear theory, as the peculiar velocity field is known to keep linear even on scales where the density contrast becomes mildly non-linear. This simplification should not be critical in simulating the spectra, as the effect of peculiar velocities results in a shift of the line and in an alteration of the profile (BD97), which will have little impact on the recovered column density of the absorber.

After having simulated the gas distribution, the photoionization code CLOUDY (Ferland et al. 1998) is used to compute the ionization states of metals. In this analysis, we have considered both the collisional ionization and the photoionization. The ionizing background consists of the sum of a UV background, arising from AGNs and galaxies, and an X-ray background, probably produced by a population of moderately X-ray luminous AGNs at $z \sim 2$ (Fabian & Barcons 1992), while for the soft X-ray part (<1 keV) a significant contribution comes from the WHIM itself (Cen et al. 1995; Phillips et al. 2001).

Among the heavy elements that can produce absorption lines in the X-rays, oxygen is the most abundant one and produces the strongest lines. A more complete treatment should also include other elements such as C, N, Ne, Fe and Si but, in our simplified scheme, we will concentrate only on oxygen lines. For a full list of resonant absorption lines, we refer the reader to Verner, Verner & Ferland (1996). We simulate absorption spectra for the two strongest transitions of the ions O VII ($E = 0.57$ keV, $\lambda = 21.6$ Å, $f = 0.7$) and O VIII ($E = 0.65$ keV, $\lambda = 18.97$ Å, $f = 0.42$), with f the oscillator strength.

The density of each ion is obtained through: $n_{\rm I}(x) = n_{\rm H}(x)\ X_{\rm I}\ Y_{\rm Z_\odot}\ Z/{\rm Z_\odot}$, where $X_{\rm I}$ is the ionization fraction of the ion as determined by CLOUDY and depends on gas temperature, gas density and ionizing background, $n_{\rm H}$ is the density of hydrogen atoms, Z is the metallicity of the element and $Y_{\rm Z\odot}$ is the solar abundance of the element. In Fig. 4 we plot the ionization fraction for O VII and O VIII as a function of the temperature for two different values of the IGM density corresponding to an overdensity $\delta_{\rm IGM} = 6$ (left-hand panel) and $\delta_{\rm IGM} = 120$ (right-hand panel), corresponding to densities of 1.4×10^{-6} cm^{-3} and 3×10^{-5} cm^{-3}. To check if the metals considered here are in photoionization equilibrium, we compute the recombination time $t_{\rm rec} = (n_{\rm IGM}\ \alpha_{\rm rec})^{-1}$, with $\alpha_{\rm rec}$ the recombination rate. For O VII and O VIII in the temperature ranges considered here, one has that $\alpha_{\rm rec} \sim 2 \times 10^{-11}$ cm^3 s^{-1} (Mazzotta et al. 1998), where both the dielectronic and radiative recombinations are taken into account. This means that the Hubble time is larger than the recombination time roughly for densities $\gtrsim 10^{-7}$ cm^{-3}. Thus, for the WHIM, the approximation of photoionization equilibrium should be reasonable.

Given the density of a given ion along the LOS, the optical depth in redshift-space at velocity u (in km s^{-1}) is

$$\tau_{\rm I}(u) = \frac{\sigma_{0,\rm I} c}{H(z)} \int_{-\infty}^{\infty} {\rm d}y\, n_{\rm I}(y) \mathcal{V}\left[u - y - v_\parallel^{\rm I}(y), b(y)\right] \qquad (3)$$

where $\sigma_{0,\rm I}$ is the cross-section for the resonant absorption and depends on $\lambda_{\rm I}$ and $f_{\rm I}$, y is the real-space coordinate (in km s^{-1}), $\mathcal{V}$ is the standard Voigt profile normalized in real-space, $b = (2k_{\rm B}\ T/m_{\rm I}c^2)^{1/2}$ is the thermal width and we assume that $v_{\rm I} = v_{\rm IGM}$. Velocity v and redshift z are related through ${\rm d}\lambda/\lambda = {\rm d}v/c$, where $\lambda = \lambda_{\rm I}\ (1 + z)$. For the low-column-density systems considered here, the Voigt profile is well approximated by a Gaussian: $\mathcal{V} = (\sqrt{\pi}b)^{-1} \exp\{-[u - y - v_\parallel^{\rm I}(y)]^2/b^2\}$. The X-ray optical depth τ will be the sum of the source continuum, which we assume we can determine, and that of equation (3). Finally, the transmitted flux is simply $\mathcal{F} = \exp(-\tau)$.

We generate 400 spectra with our semi-analytical technique at a median redshift of $z \sim 0.05$ and ∼12 000 km s^{-1} long. Both for the semi-analytical model and for the hydro-simulations, spectra have been produced with a resolution of ∼3 km s^{-1}. The goal is to reproduce the number and characteristic sizes of these absorbers with the simulation of AGN spectra by a simple semi-analytical recipe, and address their detectability. Fig. 5 shows the O VII distribution at $z = 0$ extracted from the hydro-simulation. We can see that the

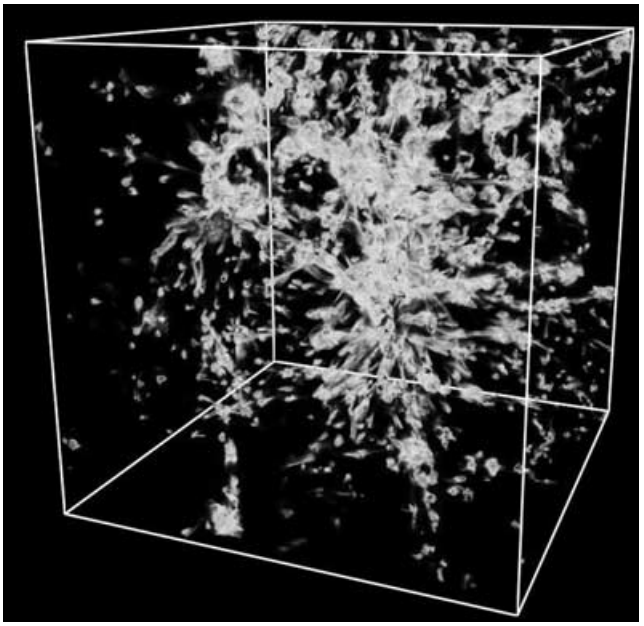

Figure 5. O VII distribution from the $z = 0$ output of the hydro-simulation (ΛCDM model, Cen et al. 2001). O VII results in a network of diffuse blobs and filaments connecting high-density regions.

O VII connects high-density regions and displays a network of filaments and diffuse blobs. From this figure we can argue that strong absorptions arise in virialized halos, while the weaker ones, possibly detected by future X-ray missions, sample filaments connecting high-density regions. The O VIII distribution is quite similar to the O VII one (Chen et al. 2002).

3 TESTING SEMI-ANALYTICAL MODELS WITH HYDRODYNAMICAL SIMULATIONS

In this Section we show how well the semi-analytical model works, after having calibrated it with the inputs obtained from hydrodynamical simulations: the pdf of the gas, the gas density–temperature relation and the gas density–metallicity relation (with the relative scatter) and the X-ray background. We compare the column-density distribution function for O VII and O VIII predicted by the semi-analytical model with those extracted directly from the hydrodynamical simulations. To this aim, the SA method has been run cutting off the large-scale power for scales larger than the box-size of the hydro-simulation (25 h^{-1} Mpc). This allows a more direct comparison between the hydro-simulation and the semi-analytical model. We checked that the statistics considered here are only marginally influenced by this assumption by running another set of SA spectra without the cut in the power spectrum. We conclude that the box-size of the hydro-simulations is large enough to study these absorbers reliably. Column densities have been computed by directly integrating the simulated optical depth and not using any fitting routine available, both for the hydro-simulations and for the SA method. Usually, the number of absorbers found is small and they can be very easily identified in our mock spectra. However, we checked that the estimated column densities are generally in good agreement with the more accurate results obtained with fitting routines.

In Fig. 6 we show the cumulative number of absorbers per unit redshift range as a function of their column density (bottom axis), i.e. the number of systems with column density larger than a given value, and as a function of the corresponding equivalent width (top axis), for O VII (left-hand panel) and O VIII (right-hand panel): the continuous lines represent the results obtained from hydrodynamical simulations, while the points are from the SA method. The absorption equivalent width, in velocity units, is related to the column density by the simple relation:

$$W = \frac{\pi e^2}{(m_e c)} \lambda f N \tag{4}$$

where N is the column density, f the oscillator strength and λ the wavelength of the transition (Sarazin 1989; Chen et al. 2002). This relation holds formally in the limit of an optically-thin absorber but is also a good approximation for column densities smaller than 10^{15} cm^{-2}.

To quantify the role of the scatter in our simulations, we decided to run another set of SA spectra and switch-off any form of scatter, both in the temperature and metallicity. Results without scatter are shown as empty circles, while those that include the scatter are represented by filled circles. From Fig. 6 we see that, when the scatter is considered, the agreement between hydro-simulations and SA is good. A first conclusion is that the inputs we used for the SA method, taken from hydro-simulations, are enough to have a good description of the number of absorbers per unit redshift range for the column-density range $10^{12.5}$ cm^{-2} $< N_{\rm OVII,OVIII} <$ $10^{15.5}$ cm^{-2}, corresponding to 0.1 km s^{-1} $\lesssim W \lesssim$ 35 km s^{-1} for $O_{\rm VII}$.

The values found are in agreement with the column-density distributions of Chen et al. (2002), which are reported in Fig. 6 and are represented as a dashed line. In the case in which they take into account the metallicity–density relation, parametrized by $\langle \log Z/Z_\odot \rangle = -1.66 + 0.36 \log \delta$, and consider a scatter drawn randomly from a lognormal distribution with $\langle \log Z/Z_\odot \rangle = -1$ and $\sigma_{\log Z} = 0.4$, the results are quite similar. We note a slightly steeper column-density distribution function in our analysis compared with the one in Chen et al. (2002), which results in a smaller number of absorbers at intermediate column densities in the range 10^{13}–10^{15} cm^{-2}. This is probably determined by the fact that our gas density–metallicity relation predicts lower metallicities than the one they used.

Before considering the detectability of these systems, we comment upon the effects of the scatter. If we do not take into account the scatter, we cannot reproduce all the systems at column densities larger than 10^{14} cm^{-2} for both the ions. For smaller column densities, the effect of the scatter is smaller but it seems that also in this range the scatter produces an increase in the number of systems.

We checked the different role played by the metallicity and temperature scatter by running another set of SA spectra switching off only one of them. It turns out that the scatter that influences most the column density of the absorbers is the one in metallicity. This is probably due to the fact that the column density of the absorbers is directly proportional to the gas metallicity (Section 2.2). The dependence on the temperature is in a sense less direct, as the latter determines the ionization fraction, computed with CLOUDY including both the collisional ionization and the photoionization contributions (see Section 2.2), which depends on the particular X-ray background chosen in a non-trivial way (see for example Fig. 4). Another reason could be that the scatter in metallicity is slightly larger than the scatter in temperature for regions with $5 < \delta < 10$, a low-density WHIM, which is responsible for a significant fraction of the absorptions.

We expect $\gtrsim$30 O VII systems with column densities larger than 10^{13} cm^{-2} corresponding to equivalent widths larger than 2 km s^{-1}, per unit redshift range at $z \sim 0$. While the number of systems with column densities larger than $10^{14.5}$ cm^{-2}, corresponding to

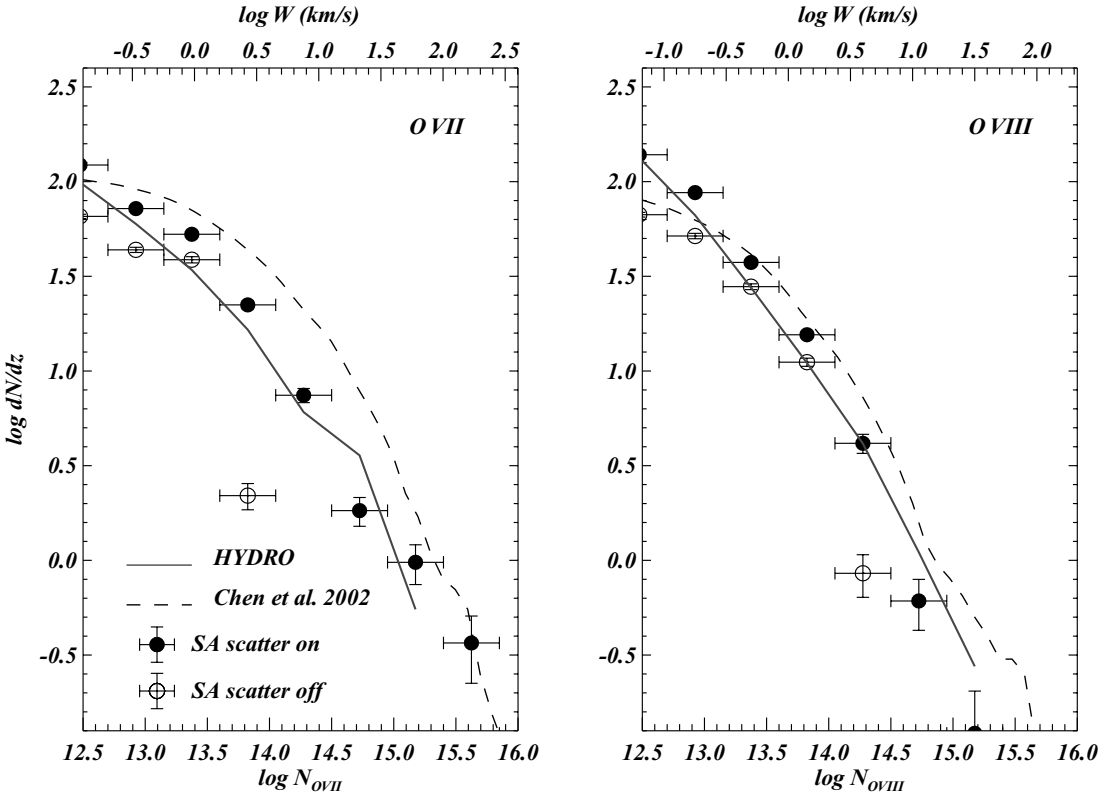

Figure 6. The left-hand panel shows the cumulative column-density distribution function for O VII (number of absorbers with column density larger than a given value per unit redshift). Filled circles are from the semi-analytical model with the scatter (i.e. implementing both the scatter in the temperature–density relation and in the density–metallicity relation in the model), empty circles are from the semi-analytical model without considering the scatter. The continuous line represents the result obtained from hydro-simulations. The dashed line shows the results of Chen et al. (2002), for a model that contains scatter in the metallicity and a trend of mean metallicity with gas overdensity: $\langle \log Z/Z_{\odot} \rangle = -1.66 + 0.36 \log \delta$. The right-hand panel shows the same quantities for O VIII. Error bars are Poissonian.

equivalent widths larger than $\sim$10 km s^{-1}, drops to five. The number of O VIII systems is similar to that of O VII ones showing that both ions trace structures at the same density, but the corresponding O VIII equivalent width is almost a factor of two lower.

4 RESULTS

To understand better the physical state of the gas that determines the absorptions, we plot in Figs 7 and 8 two AGN pairs, for two different separations of 0.2 h^{-1} Mpc and 1.2 comoving h^{-1} Mpc (the continuous line and the dashed line represent the two members of the pair) simulated with the semi-analytical technique. Assuming that the absorbers are placed at a median redshift of $z \sim 0.05$, these distances correspond to an angular separation of $\sim$3.5 arcmin and $\sim$42 arcmin, respectively, for a ΛCDM universe. If the absorbers are placed at a median redshift of $z \sim 0.1$, the angular separation is $\sim$2 arcmin and $\sim$30 arcmin, respectively.

In Figs 7 and 8 it is possible to see that the absorptions arise from gas at a temperature larger than 10^5 K which has a density larger than 10^{-6} cm^{-3}, i.e. overdensity $\delta > 6$. One can see that, while for the smaller separation (Fig. 7) the two AGNs show almost identical features both in density and temperature, which determine very similar spectra for O VII and O VIII, for the largest separation of Fig. 8 the differences are larger. This is due to the fact that now the correlations are weaker, resulting in more different density and temperature profiles for the two AGN spectra. Also the spectra now show some coincident absorptions, for example at 5600 km s^{-1}, and some anticoincidences, such as the strong one at $\sim$10 000 km s^{-1}, while at smaller separations there are only coincident features (Fig. 7).

To quantify the amount of correlation between the spectra of the AGNs of the simulated pairs we use the 'hits-and-misses' statistics described by McGill (1990), Bechtold et al. (1994), Crotts et al. (1994) and Charlton et al. (1997). A coincidence is defined as the case in which an absorption line is present in both the spectra within a given velocity difference Δv and above some signal-to-noise ratio. An anticoincidence is defined when a line is present in one spectrum but not in the other one. If there are two lines within Δv, a pretty rare event given the incidence of O VII and O VIII absorbers, we count only one coincidence and no anticoincidence, as in Fang et al. (1996). We also generate a set of spectra uncorrelated in the transverse direction and compute the same statistics to take into account the level of random coincidences. Despite the arbitrariness of the definition, which involves the choice of a velocity binning for the spectra, it has been shown that it is still useful to define a characteristic size for the observed Lyα absorbers (Fang et al. 1996; Charlton et al. 1997). The inferred 'characteristic size' of the Lyα clouds is in agreement with the results of other hydrodynamical simulations (Theuns et al. 1998) and with semi-analytical models of the Lyα forest (Viel et al. 2002a,b).

Results are shown in Fig. 9 where we plot the coefficient $f_{\rm co}$, the fraction of coincidences, which is defined as the ratio between

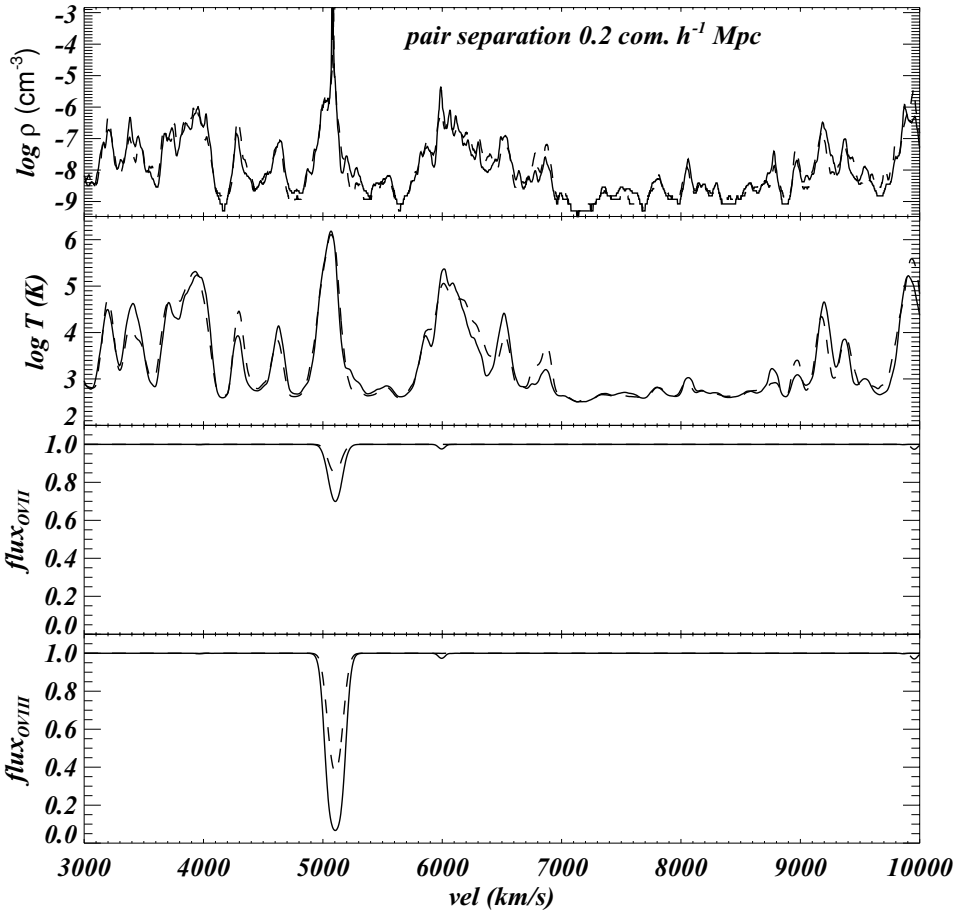

Figure 7. From top to bottom: gas density along the line of sight, temperature, spectrum for O VII and spectrum for O VIII. Continuous line and dashed line represent the two AGN spectra of a pair with separation $r_\perp = 0.2$ comoving h^{-1} Mpc at $z \sim 0.05$, simulated with the semi-analytical technique described in the text. This portion of the spectrum has been selected around one of the strongest absorptions.

the number of 'hits' and the total number of 'hits' and 'misses': the larger the value of this coefficient the larger the correlation between the two spectra. These plots have been obtained by simulating absorption spectra of 20 AGN pairs at a median redshift of $z \sim 0.05$ for 12 different separations, spanning the range 0.1–2 comoving h^{-1} Mpc, i.e angular separations from 3 to 70 arcmin. O VII and O VIII absorbers are represented by empty and filled circles, respectively. This coefficient has been computed *only for absorbers with column densities* $>10^{13}$ cm^{-2}, which will be detectable by *XEUS* and *Constellation-X*. We have decided to show this result selecting all the absorbers detectable by future X-ray missions, i.e. all the absorbers with column densities larger than 10^{13} cm^{-2}. This assumption is not crucial: the values assumed by the coefficient $f_{\rm co}$ are pretty robust and change significantly only if we include the absorbers with lower column densities. In fact, for these absorbers the level of random coincidences is higher and determines higher values of $f_{\rm co}$. The values assumed by $f_{\rm co}$ are mainly determined by the absorbers with column densities in the range $10^{13.5}$–10^{15} cm^{-2}. For larger column densities, $f_{\rm co}$ becomes smaller because the number of random coincidences found is smaller.

In the left-hand panel a bin in velocity of 100 km s^{-1} has been chosen for the hits-and-misses statistics, while in the right one the bin is of 200 km s^{-1}. The dashed line is the level of random coincidences calculated from the 'hits-and-misses' analysis of fully uncorrelated AGN spectra. For both absorbers the coefficient peaks within $\sim$0.2 comoving h^{-1} Mpc and then drops. In both panels the value at which the coefficient becomes comparable to the random coincidence level is at $\sim$1.2 comoving h^{-1} Mpc. Of course the number of random coincidences depends on the binning chosen, being smaller for smaller Δv. However, we stress that the number of random coincidences is very small, given the small number of systems expected per unit redshift path.

Assuming that the noise level for $f_{\rm co}$ is of the order of 0.05, which we can infer from the right-hand panel of Fig. 9, a 3σ detection of this filamentary structure will require at least 20 pairs with separations $\lesssim$1 comoving h^{-1} Mpc corresponding to the range $\lesssim$20 arcmin if the absorbers are placed at $z \lesssim 0.1$. Another conclusion is that a sample of at least 20 AGN pairs with this separation is necessary to discriminate between random coincidences and 'real' signals from this filamentary structure.

4.1 *XEUS* and *Constellation-X* detectability of O VII absorbers

In this section we quantify the detectability of O VII absorbers, following the treatment and formalism of Sarazin (1989). In particular, we compute detection thresholds of the filamentary network for single AGN spectra and for AGN pairs. This means that in the latter case we will need 20 pairs of sources with separation $\lesssim$20 arcmin, in a given portion of the sky, to probe the characteristic size of the absorbers by analysing coincident absorption features (see Section 4).

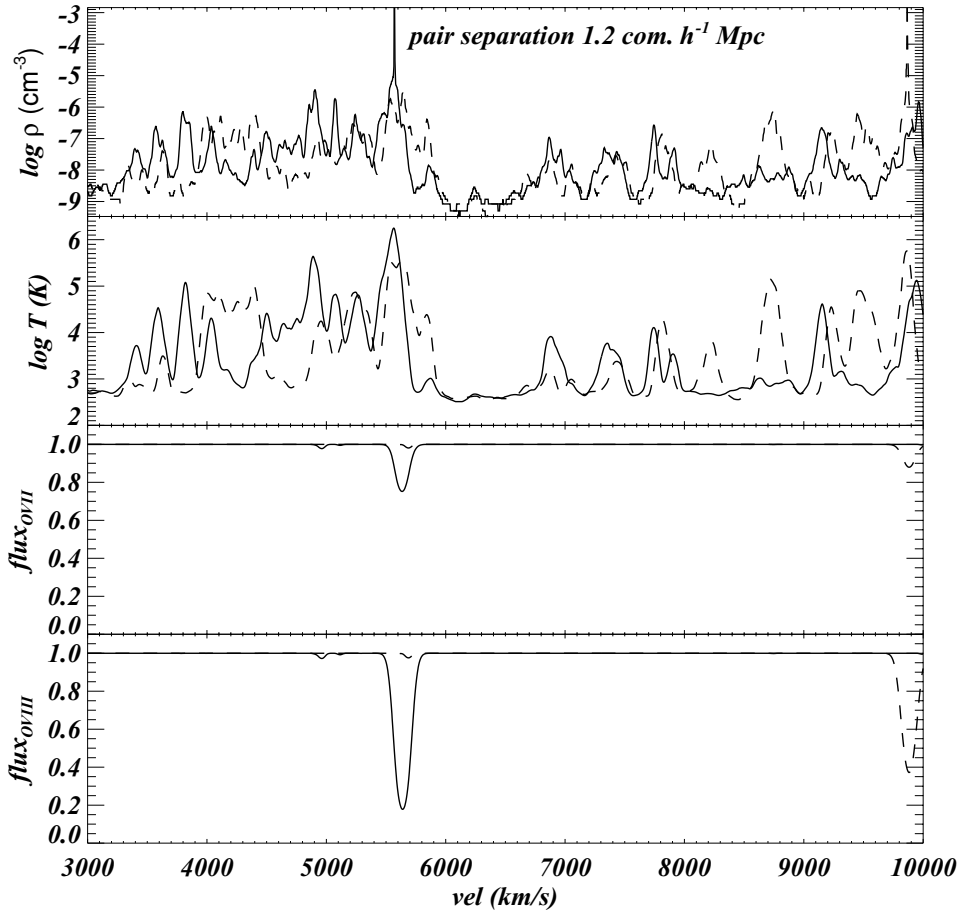

Figure 8. From top to bottom: gas density along the line of sight, temperature, spectrum for O VII and spectrum for O VIII. Continuous line and dashed line represent the two spectra of the AGN pair with a separation of $r_\perp = 1.2$ comoving h^{-1} Mpc at $z \sim 0.05$, simulated with the semi-analytical technique described in the text. This portion of the spectrum has been selected around one of the strongest absorptions.

We decided to focus only on O VII absorbers. As stressed above, O VII and O VIII absorbers probe the same structures but, for a given column density, the corresponding O VII absorber equivalent width is a factor two higher than the O VIII one. This means that O VII absorbers can probably be detected in slightly-lower-density regions than O VIII ones, so they can better trace the bulk of the filamentary structure.

In the following discussion all the fluxes are expressed in the *ROSAT* All-Sky Survey (RASS) 0.1–2.4 keV energy band.

In order to detect absorption lines with a specified signal-to-noise level *S/N*, the detector must collect, within the instrument energy resolution ΔE, a number of continuum photons given by $N_{\rm photons} \gtrsim (S/N)^2 (W_{\rm abs}/\Delta E)^{-2}$, where $W_{\rm abs}$ is the absorber equivalent width. The corresponding flux at the line energy E is:

$$F \gtrsim 1.3 \times 10^{-12} \left(\frac{E}{1\,{\rm keV}}\right)^{-1} \left(\frac{S/N}{3}\right)^{2} \left(\frac{\Delta E}{10\,{\rm eV}}\right) \times \left(\frac{W_{\rm abs}}{100\,{\rm km\,s^{-1}}}\right)^{-2} \left(\frac{AQ}{10000\,{\rm cm^2}}\right)^{-1} \times \left(\frac{t}{100\,{\rm ks}}\right)^{-1} {\rm erg\,cm^{-2}\,s^{-1}\,keV^{-1}}, \quad (5)$$

where AQ is the effective collecting area (Q is the quantum efficiency of the detector) and t is the integration time.

We estimate the source flux needed to detect O VII absorption lines ($E = 0.57$ keV, in the observer rest frame) using different X-ray telescopes and exposure times of 500 ks. Although a conservative line detection requires a $S/N = 5$, in all our calculations below we choose $S/N = 3$.

We find that the detection of these absorbers is quite difficult. The resolution and collecting areas at $\sim$0.5 keV of the present generation X-ray satellites are: $R = E/\Delta E = 500$, $AQ = 25$ cm^2 and $R = 500$ and $AQ = 70$ cm^2 for *Chandra* and *XMM–Newton*, respectively. If we substitute these values in equation (5) we find that column densities of 10^{14} cm^{-2}, corresponding to equivalent widths $W \lesssim 10$ km s^{-1}, cannot in practice be detected by these satellites: they either require exceptionally bright background sources with fluxes $\sim 10^{-9}$ erg cm^{-2} s^{-1} (calculated assuming a source spectrum $F \propto E^{-0.7}$) or unrealistic exposure times of the order of the *Chandra* lifetime. On the other hand, if we consider more realistic, although still quite bright and rare, X-ray sources with $F \sim 10^{-11}$ erg cm^{-2} s^{-1}, we find that the only observable absorption features detectable by *Chandra* and *XMM–Newton* are those with $W > 200$ km s^{-1} (see also Mathur, Weinberg & Chen 2002; Fang et al. 2002b).

Conversely, the low-density network of filaments can be detectable by next-generation satellites with much higher collecting area, such as *Constellation-X*[1] and especially *XEUS*,[2] For these

[1] http://constellation.gsfc.nasa.gov
[2] http://astro.estec.esa.nl/SA-general/Projects/XEUS

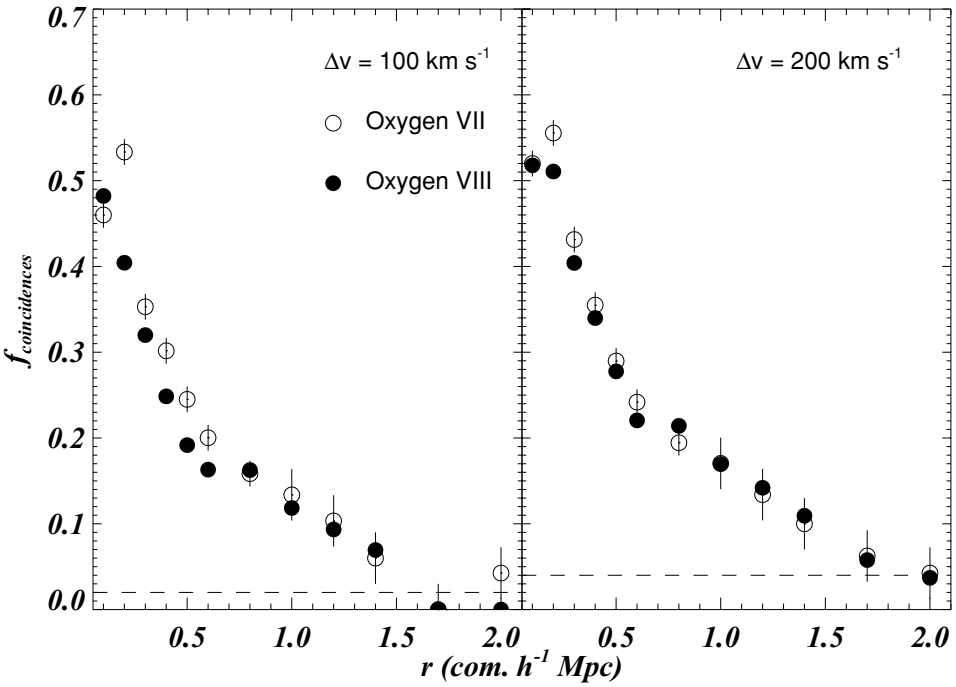

Figure 9. The coefficient representing the fraction of coincidences, as defined in the text, i.e. the number of 'hits' divided by the total number of 'hits' and 'misses', plotted as a function of the separation between the two AGNs. Only absorbers with column densities larger than 10^{13} cm^{-2}, which can be detected by *XEUS* and *Constellation-X*, have been selected to compute this coefficient. The chosen bin to compute the hits and misses statistics is $\Delta v = 100$ km s^{-1} in the left-hand panel and $\Delta v = 200$ km s^{-1} in the right one. Empty circles represent results for O VII and filled ones for O VIII. The dashed line is the level of random coincidences, which depends on the velocity bin chosen. The points have been obtained by simulating 20 pairs for each separation. Error bars (plotted only for O VII) represent the errors of the mean.

satellites the effective collecting area and resolution are: $R = 1500$, $AQ = 3000$ cm^2 for *Constellation-X* and $R = 800$ and $AQ = 40\,000$ cm^2 for *XEUS*. We mention here that the value $R = 1500$ for *Constellation-X* is that expected from the off-plane option for the Reflection Grating Spectrometer (W. Cash 2002, http://constellation.gsfc.nasa.gov) and that for *XEUS* the ultimate satellite configuration *XEUS-2* will allow one to reach an effective area of $AQ = 2 \times 10^5$ cm^2.

Assuming that sources with a flux $\sim 10^{-11}$ erg cm^{-2} s^{-1} are observed, we find that the minimum detectable equivalent widths are $\sim$6 and $\sim$3 km s^{-1} for *Constellation-X* and *XEUS*, respectively. With *XEUS-2* the minimum detectable equivalent width will be $\sim$1.5 km s^{-1}. These equivalent widths will probe the range of absorbers of column densities of $\gtrsim 10^{14.6}$ cm^{-2} for *Constellation-X*, $\gtrsim 10^{13.8}$ cm^{-2} for *XEUS* and $\gtrsim 10^{13.5}$ cm^{-2} for *XEUS-2*.

We now estimate the number of AGNs with fluxes sufficient to allow detection of absorbers of given $W_{\rm abs}$. We use the fit to the log N–log S relation $\mathcal{N}(>S) \sim 5.1 \times 10^{-16} (S/{\rm erg cm^{-2}\ s^{-1}})^{-1.5}$ sr^{-1}, originally calculated in the *Einstein* band and here renormalized to the *ROSAT* band (see Maccacaro et al. 1982; Hasinger et al. 1993). Formally this fit is valid for fluxes in the range 10^{-13}–10^{-11} erg cm^{-2} s^{-1} and extrapolation to lower fluxes can be dangerous as we know, for example, that the *ROSAT* Log N–Log S function in the Lockman Hole has a shallower slope than the one used here at lower fluxes (Hasinger et al. 1998). Nevertheless, as we are interested in very bright sources, the Maccacaro et al. fit should be a good approximation. Assuming that the typical quasar spectrum is given by $F \propto E^{-0.7}$ from equation (5) and the adopted Log N–Log S relation we find:

$$\mathcal{N}(>F) \approx 100 \left(\frac{E}{1\,{\rm keV}}\right)^{0.45} \left(\frac{S/N}{3}\right)^{-3} \left(\frac{\Delta E}{10\,{\rm eV}}\right)^{-1.5} \times \left(\frac{W_{\rm abs}}{100\,{\rm km\,s^{-1}}}\right)^{3} \left(\frac{AQ}{10000\,{\rm cm^2}}\right)^{1.5} \left(\frac{t}{100\,{\rm ks}}\right)^{1.5} {\rm sr^{-1}}. \quad (6)$$

In Fig. 10 we plot the number of sources per steradian with enough flux to allow the detection of absorbers of a given equivalent width. The solid line refers to *XEUS*, the dotted one to *XEUS-2* and the dashed one on the right refers to *Constellation-X*. In the same figure we also report the corresponding O VII column densities.

From Fig. 10 one can see that *XEUS* can detect roughly 10 sources per steradian with equivalent width $\sim$2.5 km s^{-1}, corresponding to column densities of $10^{13.8}$ cm^{-2} for O VII. For these sources, at least a number of 30 features can be seen in absorption per unit redshift range if the current models for the WHIM are correct (Fig. 8). *XEUS-2* will find a factor of 10 more sources per steradian than *XEUS*, which will allow one to probe the same WHIM structures. *Constellation-X* will not be able to probe the same very low-density range. For example, in this case 10 single sources per unit solid angle, bright enough to probe absorbers with an equivalent width of $\sim$10 km s^{-1}, are predicted to be in the sky. The number of absorption features with this equivalent width is approximately 1 per unit redshift range.

We estimate now the number of AGN pairs with flux above a given value and whose relative separation is between $\theta_{\rm min}$ and $\theta_{\rm max}$. To this aim we consider a survey area Σ and we use the X-ray sources angular correlation function $w(\theta) = (\theta/\theta_0)^{-0.8}$, with $\theta_0 \sim 3$ arcmin (Akylas, Georgantopoulos & Plionis 2000).

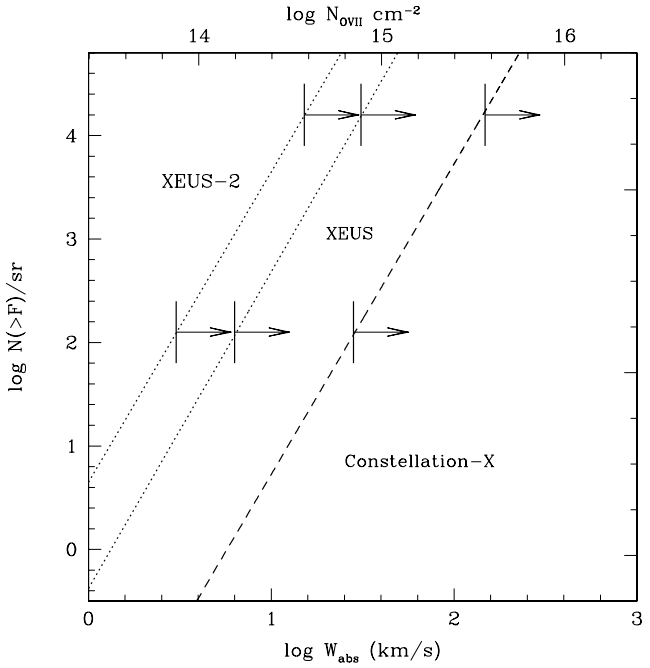

Figure 10. Cumulative source number per steradian with enough flux to allow detection of O VII absorption lines with a given equivalent width. The continuous line is for *XEUS*, the dotted one for *XEUS-2* and the dashed one for *Constellation-X*, respectively. We assumed S/N =3 and exposure times of 500 ks. Vertical lines mark thresholds for which the structures can be probed by AGN pairs. The first threshold on the left represents the estimated minimum W detectable for O VII from a sample of 20 pairs, with separation $\lesssim$ 20 arcmin, from an observation of the whole sky. The second threshold represents the same value but obtained from a sample of 20 pairs found in a smaller random field of 4 deg^2. In the upper axis the corresponding O VII column densities are reported.

If we indicate with $\mathcal{N}_\Sigma = \int_\Sigma \mathcal{N}(>F)\,\mathrm{d}\Omega$ the total number of sources in the survey with flux above a given value, then the number of distinct pairs whose members have a relative separation between $\theta_{\rm min}$ and $\theta_{\rm max}$ is:

$$\mathcal{N}_{\rm pairs}(\theta_{\rm min},\theta_{\rm max}) = \pi\mathcal{N}\mathcal{N}_\Sigma \int_{\theta_{\rm min}}^{\theta_{\rm max}} [1+w(\theta)]\sin\theta\,\mathrm{d}\theta$$
$$\approx \frac{\pi\mathcal{N}\mathcal{N}_\Sigma}{2}\left(\theta^2_{\rm max} + 1.7\,\theta_0^{0.8}\,\theta^{1.2}_{\rm max}\right), \qquad (7)$$

where the last expression is valid for small separations and for $\theta_{\rm min} = 0$.

We choose the limits $\theta_{\rm min} = 0$ and $\theta_{\rm max} = 20$ arcmin in computing the number of pairs. For these angular separations, as we have found in Section 4, we expect to find significant coincidence features in the spectra of AGN pairs.

The vertical bars in Fig. 10 represent the minimum absorber equivalent width that can be probed by using AGN pairs instead of single AGN spectra. Detection of the filamentary structure with future missions can be achieved by finding coincident absorptions in AGN pairs, as we showed in Section 4.

The first threshold on the left in Fig. 10 corresponds to the equivalent width that can be probed from a sample of 20 pairs, with the right separations, found in the whole sky, while the threshold to the right corresponds to a field of 4 deg^2. This means that, if *XEUS* or *Constellation-X* will observe a random field of 4 deg^2 in the sky, they will find 20 AGN pairs with the wanted separation with fluxes high enough to probe WHIM structures at the corresponding equivalent width. If this is the case, the expected number of O VII absorption features seen by XEUS per unit redshift range is ∼2.5. Thus, if these objects are placed at $z \sim 0.5$ we predict that a sample of 20 spectra of AGN pairs will possibly show a total of ∼50 absorption O VII features, while *Constellation-X* will detect a factor of three fewer absorption features. The more powerful *XEUS-2* will detect ∼100 absorptions in the same conditions. An observation of the whole sky will possibly allow these satellites to detect WHIM structures at smaller column densities.

To conclude, we verify if the *ROSAT* all-sky survey bright source catalogue (Voges et al. 1999) may contain the positions of a sufficient number of pairs to probe WHIM structure. This catalogue contains a sample of 18 811 sources down to a limiting *ROSAT* PSPC count-rate of 0.05 counts s^{-1} in the 0.1–2.4 keV band, which corresponds to a flux limit 5.2×10^{-13} erg cm^{-2} s^{-1} (assuming a photon spectrum that can be modelled by a power law with slope −1 and no absorption, 1 count s^{-1} ∼ 1×10^{-11} erg cm^{-2} s^{-1}). We find that the number of pairs of sources whose separation is smaller than 20 arcmin is ∼100 for fluxes larger than 3.3×10^{-12} erg cm^{-2} s^{-1}, and is ∼300 for fluxes larger than 2.2×10^{-12} erg cm^2 s^{-1}. If we consider that approximately 16 per cent of the X-ray sources have unique counterpart of extragalactic origin (Voges et al. 1999), we deduce that the RASS catalogue should contain the positions of ∼48 pairs of extra-galactic sources with fluxes $\gtrsim 2 \times 10^{-12}$ erg cm^{-2} s^{-1}. These bright sources will allow *XEUS* to probe absorbers of $W \sim 7$ km s^{-1} (see equation 5).

5 DISCUSSION AND CONCLUSIONS

In this paper we have presented a semi-analytical technique to simulate X-ray absorption spectra of distant AGNs. The warm–hot intergalactic medium (WHIM) can be detected both in absorption and in emission. Recently, a number of missions devoted to the study of the WHIM through the observation of emission lines (see, for example, the missions *SPIDR*[3] or *IMBOSS*[4]) have been proposed. Unlike the line emission process, which is proportional to the density square, the line absorption has the advantage of being proportional to the density of the intervening absorber. Furthermore, absorption measurements are not subject to background contamination. Absorption measurements, then, happen to be more sensitive than emission ones to the lower-density regions of the WHIM. Having a larger volume filling factor, these low regions constitute the bulk of the filamentary structure. Thus, absorption measurements, besides representing an important tool complementary to emission ones, are probably more promising for studying the large-scale structures traced by the WHIM.

The method proposed here uses as input four results obtained from the $z = 0$ output of large box-size ΛCDM hydrodynamical simulations: the probability distribution function of the gas, the gas temperature–density relation, and the gas metallicity–density relation. These quantities are sufficient to give a good description of the number of O VII and O VIII absorbers expected in the low-redshift Universe. Simulations of these two ions are very important: they are the strongest trace of the WHIM. If we sum up all the baryons at $z \sim 2$ and compare this value with the baryons seen at $z \sim 0$, we discover that a significant fraction of the baryons is missing (Cen &

[3] http://www.bu.edu/spidr/
[4] http://www.ias.rm.cnr.it/IMXS/iasimxs.html

Ostriker 1999). This fraction is thought to be in the WHIM. Thus, the detectability of this network of O VII and O VIII filaments is of fundamental importance.

We have extended the simulation of a line of sight (LOS) to the simulation of pairs of LOS with the mathematical implementation reported in Appendix A (see also Viel et al. 2002a). This has been done in order to give an estimate of the characteristic size of the absorbers by using the information contained in the transverse direction. While single LOSs are sensitive to the size of single absorbers, pairs of LOSs should be more reliable a probe of the network of filaments traced by the metals as they are more sensitive to the random orientation of each filament. We have performed the so-called 'hits-and-misses' statistics (McGill 1990; Charlton et al. 1997) on a sample of simulated pairs to obtain an estimate of this size.

The main result of the first part of the paper can be summarized as follows: (i) semi-analytical models successfully reproduce the number of absorbers per unit redshift path of hydrodynamical simulations and we expect $\gtrsim$30 absorbers per unit redshift with an O VII column density $>10^{13.5}$ cm^{-2}; (ii) scatter in the metallicity–gas density relation plays a significant role in increasing the number of absorbers with column densities $\gtrsim 10^{14}$ cm^{-2}; (iii) the characteristic size of these absorbers at $z \sim 0$, obtained by analysing coincident absorptions in simulated spectra of AGN pairs, is $\sim$1.

In the second part we have discussed the detectability of the absorbers by present X-ray missions, such as *Chandra* and *XMM–Newton*, and future ones, such as *XEUS* and *Constellation-X*. Up to now only few 'trees' of the 'X-ray forest' have been detected by *Chandra* (Fang et al. 2002b; Nicastro et al. 2002a). Most likely, these absorbers sample the high-column-density tail of the distribution shown in Fig. 6. A detection of the lower-column-density absorbers, whose volume filling factor is larger, can be achieved only by future X-ray missions whose collecting area and sensitivity will be higher.

We have found that at least a background of 20 pairs of bright extragalactic AGN-like sources at a median redshift of $z \sim 0.5$ and with relative separations lower than 20 arcmin is needed to probe these filamentary structures with 'hits-and-misses' statistics. We have made a theoretical estimate to address the detectability of these sources by *XEUS* and *Constellation-X* taking into account the bright X-ray sources angular correlation function (Akylas et al. 2000). The main conclusions are: (i) by observing a random field of 4 deg^2, *XEUS* and *Constellation-X* will be able to probe WHIM absorbers, with 'hits-and-misses' statistics, which will correspond to O VII column densities $10^{14.8}$ and $10^{15.5}$ cm^{-2}, respectively; (ii) in this field, *XEUS* and *XEUS-2* will possibly find $\sim$50 and $\sim$80 absorption features, respectively, if we assume that the sources are placed at a median redshift of $z \sim 0.5$; (iii) *XEUS* will detect at least 10 sources per steradian bright enough to probe structures with an absorber equivalent width of 2.5 km s^{-1}, corresponding to an O VII column density of $10^{13.8}$ cm^{-2}; (iv) *Constellation-X* will detect few thousand sources per steradian bright enough to probe structure with an equivalent width of $\sim$100 km s^{-1}. We have checked in the *ROSAT* all-sky survey bright source catalogue (Voges et al. 1999) to determine if these sources had already been detected. We have found that the required number of extragalactic sources with the necessary angular separation is present in the catalogue. Re-observation of these sources will allow future X-ray missions to detect baryons in the low-redshift Universe and to unveil the filamentary structure where they preferentially reside.

ACKNOWLEDGMENTS

We thank M. Haehnelt, V. Mainieri, G. Matt, M. Mendez, G. Perola and C. Porciani for useful discussions and technical help. We thank the anonymous referee for helpful comments and X. Chen for kindly providing his data. MV acknowledges partial financial support from an EARA Marie Curie Fellowship under contract HPMT-CT-2000-00132. This work has been partially supported by the European Community Research and Training Network 'The Physics of the Intergalactic Medium' and by Grant ASC97-40300.

REFERENCES

Akylas A., Georgantopoulos I., Plionis M., 2000, MNRAS, 318, 1036
Bechtold J., Crotts A. P. S., Duncan R. C., Fang Y., 1994, ApJ, 437, 83
Bi H. G., 1993, ApJ, 405, 479
Bi H. G., Davidsen A. F., 1997, ApJ, 479, 523 (BD97)
Bi H. G., Börner G., Chu Y., 1992, A&A, 266, 1
Bi H. G., Ge J., Fang L.-Z., 1995, ApJ, 452, 90
Boldt R., 1987, Phys. Rep., 146, 215
Burles S., Tytler D., 1998, ApJ, 499, 699
Cen R., Ostriker J. P., 1999a, ApJ, 514, 1
Cen R., Ostriker J. P., 1999b, ApJ, 519, L109
Cen R., Simcoe R. A., 1997, ApJ, 483, 8
Cen R., Miralda-Escudé J., Ostriker J. P., Rauch M., 1994, ApJ, 437, L83
Cen R., Kang H., Ostriker J. P., Ryu D., 1995, ApJ, 451, 436
Cen R., Tripp T. M., Ostriker J. P., Jenkins E. B., 2001, ApJ, 559L5
Charlton J. C., Anninos P., Zhang Y., Norman M. L., 1997, ApJ, 485, 26
Chen X., Weinberg D. H., Katz N., Davé R., 2002, ApJ, submitted (astro-ph/0203319)
Crotts A. P. S., Bechtold J., Fang Y., Duncan R. C., 1994, ApJ, 437, 79
Davé R., Hernquist L., Katz N., Weinberg D. H., 1999, ApJ, 511, 521
Davé R. et al., 2001, ApJ, 552, 473
Fabian A. C., Barcons X., 1992, ARA&A, 30, 429
Fang Y., Duncan R. C., Crotts A. P. S., Bechtold J., 1996, ApJ, 462, 77
Fang T., Bryan G. L., Canizares C. R., 2002a, ApJ, 564, 604
Fang T., Marshall H. L., Lee J. C., Davis D. S., Canizares C. R., 2002b, ApJ, 572, L127
Ferland G. J., Korista K. T., Verner D. A., Ferguson J. W., Kingdon J. B., Verner E. M., 1998, PASP, 110, 761
Fukugita M., Hogan C. J., Peebles P. J., 1998, ApJ, 503, 518
Gnedin N. Y. et al., 2003, ApJ, 583, 525
Hasinger G., Burg R., Giacconi R., Schmidt M., Trümper J., Zamorani G., 1998, A&A, 329, 482
Hasinger G., Burg R., Giacconi R., Hartner G., Schmidt M., Trümper J., Zamorani G., 1993, A&A, 275, 15
Hellsten U., Gnedin N. Y., Miralda-Escudé J., 1998, 509, 56
Kravtsov A. V., Klypin A., Hoffman Y., 2002, ApJ, 571, 563
Lahav O., Lilje P. B., Primack J. R., Rees M. J., 1991, MNRAS, 251 128
Maccacaro T. et al., 1982, ApJ, 253, 504
Matarrese S., Mohayaee R., 2002, MNRAS, 329, 37
Mathur S., Weinberg D. H., Chen X., 2002, ApJ, 582, 82
Mazzotta P., Mazzitelli G., Colafrancesco S., Vittorio N., 1998, A&AS, 133, 403
McGill C., 1990, MNRAS, 242, 544
Miralda-Escudé J., Cen R., Ostriker J. P., Rauch M., 1996, ApJ, 471, 582
Nicastro F. et al., 2002a, ApJ, 573, 157
Nicastro F. et al., 2002b, Nat, in press (astro-ph/0208012)
Ostriker J. P., Cen R., 1996, ApJ, 464, 27
Perna R., Loeb A., 1998, ApJ, 503, L135
Phillips L. A., Ostriker J. P., Cen R., 2001, ApJ, 554, 9
Press W. H., Schechter P., 1974, ApJ, 187, 425
Rauch M., 1998, ARA&A, 36, 267
Rauch M. et al., 1997, ApJ, 489, 7
Reisenegger A., Miralda-Escudé J., 1995, ApJ, 449, 476

Ricotti M., Gnedin N. Y., Shull J. M., 2000, ApJ, 534, 41
Sarazin C. L., 1989, ApJ, 345, 12
Scharf C., Donahue M., Voit G. M., Rosati P., Postman M., 2000, ApJ, 528L73
Schaye J., 2001, ApJ, 559, 507
Schaye J., Theuns T., Rauch M., Efstathiou G., Sargent W. L. W., 2000, MNRAS, 318, 817
Shull J. M., Roberts D., Giroux M. L., Penton S. V., Fardal M. A., 1999, AJ, 118, 1450
Theuns T., Leonard A., Efstathiou G., Pearce F. R., Thomas P. A., 1998, MNRAS, 301, 478
Tripp T. M., Savage B. D., Jenkins E. B., 2000, ApJ, 534, L1
Valageas P., Schaeffer R., Silk J., 2002, 388, 741
Verner D. A., Verner E. M., Ferland G. J., 1996, Atomic Data Nucl. Data Tables, 64, 1
Viel M., Matarrese S., Mo H. J., Haehnelt M. G., Theuns T., 2002a, MNRAS, 329, 848
Viel M., Matarrese S., Mo H. J., Theuns T., Haehnelt M. G., 2002b, MNRAS, 336, 685
Voges W. et al., 1999, A&A, 349, 389
Yoshida N., Stoher F., Springel V., White S. D. M, 2002, 335, 762
Zappacosta L., Mannucci F., Maiolino R., Gilli R., Ferrara A., Finoguenov A., Nagar N. M., Axon D. J., 2002, A&A, 394, 7

APPENDIX A: CORRELATION PROCEDURE TO GENERATE MULTIPLE LINES OF SIGHT DENSITY AND VELOCITY FIELDS

We briefly report here the correlation procedure of Viel et al. (2002a).

Let us start by obtaining auto and cross-spectra for the 1D random fields which are defined along single or multiple LOS. In the Gaussian case these quantities fully determine the statistical properties of the generated fields. If $\psi(\boldsymbol{x})$ is a 3D random field with Fourier transform $\psi(\boldsymbol{k})$ and 3D power spectrum $P(|k|)$, one can define the LOS random field $\psi_\parallel(x_\parallel, \boldsymbol{x}_\perp)$ as the 1D Fourier transform

$$\psi_\parallel(k_\parallel|\boldsymbol{x}_\perp) \equiv \int \frac{\mathrm{d}^2 k_\perp}{(2\pi)^2} e^{i\boldsymbol{k}_\perp\cdot\boldsymbol{x}_\perp}\psi(k_\parallel, \boldsymbol{k}_\perp). \tag{A1}$$

The cross-spectrum $\pi(|k_\parallel||r_\perp)$ for this LOS random field along parallel LOSs, separated by a transverse distance $r_\perp$, is defined by

$$\langle\psi_\parallel(k_\parallel|\boldsymbol{x}_\perp)\psi_\parallel(k'_\parallel|\boldsymbol{x}_\perp + \mathbf{r}_\perp)\rangle = 2\pi\delta_\mathrm{D}(k_\parallel + k'_\parallel)\pi(|k_\parallel||r_\perp), \tag{A2}$$

where δ_D is the Dirac delta function and $\pi(k|r_\perp)$ can be related to the 3D power spectrum as follows:

$$\pi(k|r_\perp) = \int \frac{\mathrm{d}^2 k_\perp}{(2\pi)^2} e^{i\boldsymbol{k}_\perp\cdot\mathbf{r}_\perp} P(\sqrt{k_\perp^2 + k^2}). \tag{A3}$$

Integrating over angles and shifting the integration variable yields

$$\pi(k|r_\perp) = \frac{1}{2\pi}\int_k^\infty \mathrm{d}q\, q\, J_0(r_\perp\sqrt{q^2 - k^2})P(q), \tag{A4}$$

where J_0 is the Bessel function of order 0.

In the limit of vanishing distance between the two LOSs, $J_0 \to 1$ and the above formula reduces to the standard relation for the LOS (1D) auto-spectrum in terms of the 3D power spectrum

$$p(k) \equiv \pi(k|r_\perp = 0) = \frac{1}{2\pi}\int_k^\infty \mathrm{d}q\, q\, P(q). \tag{A5}$$

Our next problem is how to generate the two random fields δ^IGM and v^IGM in 1D Fourier space ($-\infty < k_\parallel < \infty$). These random fields have non-vanishing cross-correlations but unlike their 3D Fourier space counterparts they cannot be related by simple algebraic transformations.

We can generally write any M-dimensional Gaussian random vector $\boldsymbol{V}$ with correlation matrix $\mathbf{C}$ and components $c_{ij} = \langle V_i V_j\rangle$, as a linear combination of another M-dimensional Gaussian random vector $\boldsymbol{X}$ with diagonal correlation matrix, which we can take as the identity $\mathbf{I}$ without any loss of generality. The transformation involves the $M \times M$ matrix $\mathbf{A}$, with components α_{ij}, as follows: $\boldsymbol{V} = \mathbf{A}\boldsymbol{X}$. One obtains $\mathbf{C} = \mathbf{A}\mathbf{A}^\mathrm{T}$, i.e. $c_{ij} = \sum_k \alpha_{ik}\alpha_{jk}$. There is a slight complication because $\boldsymbol{V}$ is a random vector *field* defined in 1D Fourier space. We can, however, extend the above formalism to vector fields, assuming that $\boldsymbol{X}$ is a Gaussian vector field with white-noise power spectrum

$$\langle X_i(k_\parallel)X_j(k'_\parallel)\rangle = 2\pi\delta_{ij}\delta_\mathrm{D}(k_\parallel + k'_\parallel) \tag{A6}$$

(δ_{ij} is the Kronecker symbol). We then have $V_i = \sum_{j=1}^2 \alpha_{ij}X_j$ where three of the four α_{ij} components are determined by the conditions $\sum_{k=1}^2 \alpha_{ik}\alpha_{jk} = p_{ij}$. The remaining freedom (due to the symmetry of the original correlation matrix) can be used to simplify the calculations.

It is straightforward to extend our formalism to simulate the IGM properties along parallel lines of sight. Let $\boldsymbol{V}(k_\parallel)$ and $\boldsymbol{W}(k_\parallel)$ be two 1D Gaussian random vector fields obtained as in Section 2, each with the same set of coefficients α_{ij} but starting from two independent white-noise vector fields $\boldsymbol{X}$ and $\boldsymbol{Y}$ (i.e. such that $\langle X_i Y_j\rangle = 0$). Then both $\boldsymbol{V}$ and $\boldsymbol{W}$ have the correct LOS auto-spectra by construction while their mutual cross-spectra vanish: $\langle V_i(k_\parallel)W_j(k'_\parallel)\rangle = 0$.

Let us further define a new vector $\boldsymbol{V}'(k_\parallel|r_\perp)$ with components $V'_i = \sum_{k=1}^2(\beta_{ik}V_k = \gamma_{ik}W_k)$, such that its auto and cross-spectra components are given by

$$\left.\begin{aligned}\langle V_i(k_\parallel)V_j(k'_\parallel)\rangle &= \langle V'_i(k_\parallel|r_\perp)V'_j(k'_\parallel|r_\perp)\rangle \\ &= 2\pi\delta_\mathrm{D}(k_\parallel + k'_\parallel)p_{ij}(|k_\parallel|), \\ \langle V_i(k_\parallel)V'_j(k'_\parallel|r_\perp)\rangle &= 2\pi\delta_\mathrm{D}(k_\parallel + k'_\parallel)\pi_{ij}(|k_\parallel||r_\perp).\end{aligned}\right\} \tag{A7}$$

The vectors $\boldsymbol{V}$ and $\boldsymbol{V}'$ will then represent our physical IGM linear fields on parallel LOSs at a distance $r_\perp$. They will be statistically indistinguishable from those obtained by drawing two parallel LOSs separated by $r_\perp$ in a 3D realization of the linear IGM density and velocity fields.

The transformation coefficients are determined by the equations $\sum_{k,\ell=1}^2(\beta_{ik}\beta_{j\ell} = \gamma_{ik}\gamma_{j\ell})p_{k\ell} = p_{ij}$ and $\sum_{k=1}^2 \beta_{ik}p_{kj} = \pi_{ij}$. A complete set of coefficients can be found in Viel et al. (2002a).

This paper has been typeset from a TEX/LATEX file prepared by the author.